RSC Advances

PAPER

View Article Online
View Journal | View Issue

Cite this: *RSC Adv.*, 2021, **11**, 37744

Highly sensitive humidity-driven actuators based on metal–organic frameworks incorporating thermoplastic polyurethane with gradient polymer distribution†

Yi He,[a] Jiayu Guo, *[a] Xiazhen Yang,[b] Bing Guo*[a] and Hangyan Shen[a]

Ambient humidity plays an important role in the fields of industrial and agricultural production, food and drug storage, climate monitoring, and maintenance of precision instruments. To sense and control humidity, humidity-responsive actuators that mimick humidity responsive behavior existing in nature, have attracted intense attention. The most common and important class of humidity actuators is active bilayer structures. However, such bilayer structures generally show weak interfacial adhesion, tending to delaminate during frequent bending and restoration cycles. In this work, to address this problem, a novel monolayer humidity-driven actuator with no adhesive issue is developed by integrating the swellable metal–organic frameworks (MIL-88A) into thermoplastic polyurethane films. The proposed actuators display excellent humidity response that under the conditions of relative humidity simulated with saturated salt solution, the MIL-88A/polyurethane composite films show good self-folding response and stability for recycling use. In addition, a deep insight into the self-folding of the composite films is also provided and a new response mechanism is proposed. In this case, the results show that both the preparation method and response properties of the humidity actuators are improved. Therefore, it suggests a new promising way to develop and design flexible humidity actuators.

Received 8th November 2021
Accepted 11th November 2021

DOI: 10.1039/d1ra08174h

rsc.li/rsc-advances

Introduction

In nature, many organisms instinctively respond to external stimuli to defend against external invasion, prey or reduce nutrient loss and other purposes.[1–3] These ubiquitous stress response mechanisms enable biological structures to translate physical or chemical signals into macro-movements, changing shape, size, or other properties in response to environmental stimuli. These mechanisms play a crucial role in many biological processes.[4] For example, some of the leaves of Mimosa will close up in pairs when stimulated by contact, vibration, *etc.* If the stimulus is stronger, the leaves of the whole plant will even close up, with a speed of up to 15 mm s^{-1}. The leaves of Venus flycatchers can sense insects and close within a second to effectively capture prey by triggering shock resistance.[5] Sea cucumbers can alter the stiffness of their dermis within seconds to obtain survival advantages.[6] Recently, inspired by these attractive biological examples, various outstanding artificial intelligence actuators that can translate changes in environmental conditions into mechanical responses have attracted wide attentions.[7] Up to now, the integration of sensing, reporting and locomotion functions with intelligence actuators to enhance the intelligence has become the development trend.[8] These intelligence actuators show great promise in environment monitoring,[9,10] precision medicine,[11–13] soft robotics[14,15] and encapsulation,[16,17] *etc.*

As one of the most important physical quantities, the monitoring and control of ambient humidity plays an important role in the fields of industrial and agricultural production, food and drug storage, climate monitoring and maintenance of precision instruments.[18–22] Generally, the most common important structure of a humidity actuator is bilayer, which consists of an active layer and an inactive layer that differ in their hygroexpansion properties, generating a bending motion.[23–25] The reported materials for active layer are electroactive polymers (EAPs),[26,27] liquid crystal elastomers (LCE),[28] hydrogels,[29] sodium alginate,[30] paper coated with MXene,[31] carbon nanotube,[32] graphene oxide (GO)[33] or toner,[34] *etc.* Ma *et al.*[35] fabricated a humidity-responsive walking device using a poly(acrylic acid) (PAA)/poly(allylamine hydrochloride) (PAH) film as the upper active layer and a UV-cured Norland Optical Adhesive 63 (NOA 63) as the underlying layer. The cross-linked PAA/PAH layer has great ability to adsorb/desorb water molecules with increasing/decreasing environmental humidity.

[a]*College of Materials and Chemistry, China Jiliang University, Hangzhou 310018, PR China. E-mail: guojiayu2000@hotmail.com; 08b0506047@cjlu.edu.cn*

[b]*The Institute of Industrial Catalysis, Zhejiang University of Technology, Hangzhou 310032, PR China*

† Electronic supplementary information (ESI) available. See DOI: 10.1039/d1ra08174h

When the relative humidity (RH) was decreased from 12% to 5%, the upper PAA/PAH layer contracted as it lost adsorbed water molecules and the NOA63 layer remained unchanged. This large mismatch in contraction led the bilayer film to bend clockwise to nearly 180° within 9 s. Furthermore, when the RH was increased to its original level (12%), the bilayer film returned to its initial shape within 27 s. The load output by the actuator was 0.375 mN, which was 128 times larger than the weight of the actuator. Li *et al.*[36] reported a humidity-responsive caterpillar-mimetic bilayer actuator based on a wrinkled polydimethylsiloxane elastomer decorated with a hydro-responsive polyelectrolyte brush. The bilayer structure was prepared by oxygen plasma treatment onto a uniaxially pre-stretched polydimethylsiloxane (PDMS) sheet, which led to the formation of a thin and stiff sheet lying on top of the soft and thick PDMS at outer surface region. After removing the strain the PDMS sheet was then modified on one single side, by growing a polyelectrolyte brush of poly(3-sulfopropyl methacrylate potassium salt) (PSPMA) on the surface, turning the hydrophobic PDMS into hydrophilic one. Interestingly, these self-folding films can fold ultrafast into complex 3D structures upon a change in the RH of the surrounding air and can perform active movement on surfaces with a roughness gradient. Zheng *et al.*[37] demonstrated a preparation of humidity-responsive bilayer actuators with the same materials for the actuating and supporting layers to avoid the low adhesive issue of bilayer actuators during frequent usage. This kind of bilayer actuators comprises nonporous and porous PAA/PAH films that act as actuating and supporting layers, respectively. The nonporous PAA/PAH layer can absorb water molecules to expand in an environment with increased RH. Meanwhile, the pores of the porous PAA/PAH layer can provide free volume to suppress the expansion of the film after adsorption of water molecules in increased RH. However, such humidity actuators with bilayer structures generally show weak interfacial adhesion, tending to delaminate during frequent bending and restoration cycles. Moreover, shape-transformations of bilayers are limited to self-rolling structures,[38] which precludes creation of 3D architectures of greater complexity. Thus, a more convenient approach to design custom morphable 3D objects is to fabricate monolayer actuators for their industrial applications. Pan *et al.*[39] designed and manipulated the microstructure of GO films to fabricate a humidity actuator with a sole asymmetric graphene oxide (AGO) film. The AGO film was responsive to moisture and showed a maximum bending angle change of ≈1800°, exhibiting a superior bending capability. Troyano *et al.*[38,40] incorporated crystals of the flexible MIL-88A metal organic frameworks (MOFs) into a polyvinylidene fluoride (PVDF) matrix and fabricated a humidity actuator by a drop-casting method. It shows a shape-memory effect at relative humidity values from 60% to 90% and undergoes reversible shape transformations upon exposure to polar solvents and vapors. They also used a chemical etching method to generate a vertical gradient of MOFs crystals within the PVDF film, enhancing folding response and programmable self-folding deformation of the actuator. The results show that a unique and programmable self-folding deformation of the polymer film can be achieved through controlling the gradient distribution or microstructure of the breathing MOFs particles. Xu *et al.*[41] applied an acoustic field-assisted projection stereolithographic (A-PSL) process to prepare self-folding MIL-53 (Fe) composite films. The gradient distribution or microstructure of breathing MOFs was controlled by acoustic manipulation, achieving controllable self-folding deformation direction of the polymer films.

MOFs composites are a promising candidate for flexible humidity actuators since they have comprehensive performance of MOFs and polymers. On one hand, in the past decade MOFs have been used extensively for the fabrication of chemical sensors and biosensors in combination with the solid-state devices.[42–47] As a flexible MOFs series, MIL-88(Fe) (MIL = Materials from Institute Lavoisier) has attracted widespread attentions because of its ability that the unit-cell volume can reversibly increase after absorbing the polar solvent molecules due to the hydrogen bond interaction between the guest molecule and the skeleton.[48,49] However, their application for humidity actuators has been barely researched. On the other hand, thermoplastic polyurethane (TPU), a multisegmented copolymer, not only has excellent physical and chemical properties, such as excellent flexibility, elasticity and good vibration resistance, but also has biodegradable environmental protection characteristics. It has been widely used in medical and health, electronic appliances and other aspects.[50] Hence, the combination between MIL-88 series and TPU can provide a new way to design and develop environmentally friendly high-performance humidity actuators with flexibility property. To the best of our knowledge, no MOFs-based mixed matrix films with TPU serving as a binder have been reported for the humidity actuators. Thus, in this work, to make a step forward the MOFs-based humidity actuators, a simple drop-coating process was proposed to prepare humidity actuators with a single-layer structure film called MIL-88A@TPU films without a reported A-PSL or HCl etching process. The composite films were prepared by a MIL-88A-based ink consisting of MIL-88A as the core swell part and TPU as the body material. A rotary evaporation method was introduced to evaporate solvent and better disperse MIL-88A. The scope of this work is to demonstrate the feasibility of MIL-88A@TPU films to response to humidity with high sensitivity. To intuitively evaluate the moisture response of the MIL-88A@TPU films, we track the adsorption/desorption processes between 10% RH and 90% RH humidity. In fact, it can readily readopt their initial planar shape through hair dryer. In addition, we investigate the different shape changes of the MIL-88A@TPU films under different bending and restoration cycles. Moreover, a new response mechanism is proposed to validate the bending and restoration processes for the MIL-88A@TPU films.

Experimental

Materials

All solvents and reagents were purchased from commercial suppliers. All chemicals were of analytical grade and used without further purification. TPU (BASF Elastollan Soft 35A) were purchased from BASF Co., Ltd. Fumaric acid ($C_4H_4O_4$) and

PVP (M8000 k16-18) were purchased from Shanghai Aladdin Biochemical Technology Co., Ltd. $FeCl_3 \cdot 6H_2O$, *N*,*N*-dimethylformamide (DMF), methyl alcohol and ethyl alcohol were purchased from Shanghai Macklin Biochemical Co., Ltd. Water used in all experiments was deionized.

Synthetic procedures

Synthesis of MIL-88A(Fe). The MIL-88A(Fe) was synthesized following literature procedure.[51–53] Briefly, iron(III) chloride hexahydrate ($FeCl_3 \cdot 6H_2O$) (1.35 g, 5 mmol), fumaric acid (0.58 g, 5 mmol) and PVP (1.5 g) were firstly dissolved in 10 mL *N*,*N*-dimethylformamide (DMF). The solution was then transferred to a Teflon-lined stainless steel Parr bomb with 30 min vigorous stirring and heated in a draught drying oven at 85 °C for 16 h. After cooling, the resultant brown precipitate was collected by centrifugation, washed thoroughly with DMF and methanol, and dried overnight under vacuum at 80 °C.

Preparation of homogeneous MIL-88A@TPU films

For a typical MIL-88A@TPU formulation with 60 wt% of MIL-88A, 0.3 g dry MIL-88A powders were dispersed in 5 mL ethanol with bath sonication for 10 min in a scintillation vial. 0.2 g of TPU solution (dissolved in 5 mL DMF at 50 °C for 30 min) was then added into the above MIL-88A suspension such that the final MIL-88A:TPU ratio was 3 : 2 w/w. The combined MIL-88A/TPU suspension was then sonicated for 10 min in an ultrasonic bath, after which the ethanol was removed by rotary evaporation, resulting in a MIL-88A ink of MOFs and TPU in DMF. 1 mL of the prepared inks was drop casted onto a quartz slide (25 × 25 mm) and the solvent was evaporated off at 80 °C in an oven for 120 min. Finally, the resulting MIL-88A@TPU film was detached from the quartz substrate by immersion in water, washed thoroughly with ethanol, and air dried.

Measurement of humidity response performance

The humidity response performance of the actuator was analyzed by measuring the change in curvature in response to the RH varying from 30% to 90%. According to the RH table of the saturated salt solution, five different saturated salt solutions were prepared to represent the corresponding humidity at 30 °C, respectively (see Table S1†). A square glass jar containing 50 mL of the saturated salt solution was placed in an oven, where the temperature was always kept at 30 °C. The prepared MIL-88A@TPU film was suspended in the glass jar during the humidity response performance evaluation and the change in the curvature of the composite film was monitored using a phone.

Measurement of cyclic humidity response performance

The MIL-88A@TPU films were dried at 80 °C for 30 min before humidity response cycling, then suspended in a glass bottle containing NaCl saturated solution and placed at 30 °C for 10 min. The composite film was then taken out and dried at 80 °C for 5 min. During repeating the experiment 20 times, the change in the curvature of the films was monitored using a phone.

Characterization

Powder X-ray diffraction (XRD) patterns under ambient condition were collected on a Rigaku SmartlabSE X-ray diffractometer at 40 kV, 40 mA for Cu Ka ($l = 1.5418$ Å), with a scan speed of 2 s per step, a step size of 0.05° in 2θ, and a 2θ range of 5–50°. Field-emission scanning electron microscopy (FESEM) images and energy dispersive X-ray (EDS) mapping were taken with a ZEISS GeminiSEM 500 scanning electron microscope, using aluminium as a support. The Brunauer–Emmett–Teller (BET) surface calculations were carried out from N_2 adsorption–desorption isotherms measured by Micromeritics ASAP2010 at liquid nitrogen temperature (77 K) after dehydration under vacuum at 393 K for 8 h.

Results and discussion

Design and preparation of the MIL-88A@TPU films

Typically, the MIL-88A@TPU films with stable and flexible properties, were fabricated from MIL-88A inks prepared with pre-dispersion of MIL-88A in ethanol and subsequent addition of TPU solution using a modified method according to the previous reports.[54] Hence, we started by synthesizing MIL-88A crystals, using a surfactant-assisted method. These sub-micrometer-sized MIL-88A crystals (Fig. S1 and S2†) were then used to fabricate MIL-88A@TPU films with a wide range of MIL-88A loading contents from 40 wt% to 90 wt%. The MIL-88A@TPU film with *x* wt% of MIL-88A is named as xMIL-88A@TPU. The schematic diagram illustrating the fabrication process of the MIL-88A@TPU films was presented in Fig. 1. The TPU/DMF solution was added to the MIL-88A pre-dispersed in the ethanol solution and ultrasonically treated, followed by rotary evaporation to remove the ethanol, thereby obtaining the MIL-88A inks as the drop-casting solution. As expected, pre-dispersing the MIL-88A crystal particles in the solvent can effectively reduce the agglomeration effect of the MIL-88A particles. In order to further optimize the dispersion of the MIL-88A particles, a rotary evaporation method was further used. It is noteworthy that the introduction of rotary evaporation can not only remove the solvent used to disperse the MIL-88A particles, but also make the MIL-88A and TPU phase more uniformly in the DMF solution.

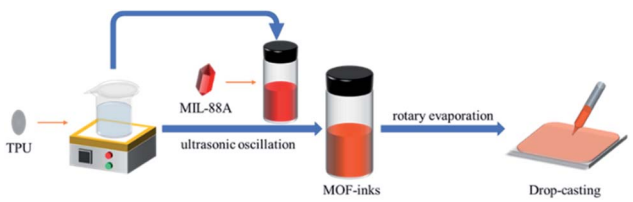

Fig. 1 The schematic diagram illustrating the preparation process of the MIL-88A@TPU films.

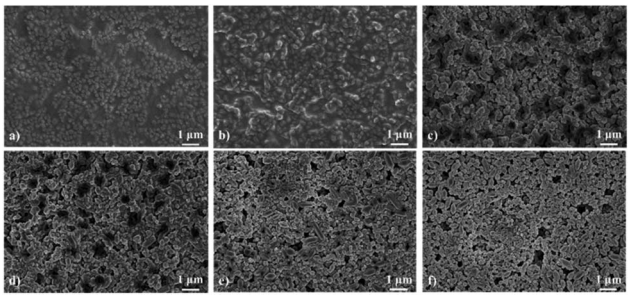

Fig. 2 FESEM images of the MIL-88A@TPU films with different MIL-88A loadings. (a) 40 wt%; (b) 50 wt%; (c) 60 wt%; (d) 70 wt%; (e) 80 wt%; (f) 90 wt%.

Morphology and microstructure of the MIL-88A@TPU films

To investigate the effects of MOF loading contents on the film morphology and microstructure, the MIL-88A@TPU films with varying MIL-88A loadings were characterized by FESEM. The FESEM (seen in Fig. 2) analyses have revealed the formation of a uniform with an isotropic distribution of the MIL-88A crystals inside the entire composite film. At low loadings of MIL-88A crystals, we have observed that there are essentially no macro-voids between the MIL-88A and the TPU phase, and that the TPU phase fills the voids among the MIL-88A particles and coats the surface of the MIL-88A particles. With increasing the MIL-88A loadings (≥60 wt%), the MIL-88A crystallites play a dominant role in the morphology of the composite film, which leads to the appearance of obvious macropores. The fact that the crystallinity of MIL-88A crystal particles in the composite films remains unchanged was further examined by the powder X-ray diffraction results, as shown in Fig. 3. The main diffraction peaks of pristine MIL-88A are located at (010), (011) and (002) (Fig. S1†). These results are in good agreement with those reported.[55,56] It is observed that the same characteristic peak at $2\theta = 10.2^\circ$ is present for the composite films with 40 wt%, 50 wt%, 60 wt%, 70 wt%, 80 wt%, and 90 wt% MIL-88A loadings as ascribed to the (011) crystal plane of MIL-88A. Thus, the XRD patterns indicate that the microstructure of the MIL-88A is preserved in the MIL-88A@TPU films. To demonstrate that the porosity of the MIL-88A is still retained in the MIL-88A@TPU films, the N_2 adsorption–desorption isotherms for MIL-88A@TPU films with different loadings of the MIL-88A were measured at 77 K (seen in Fig. S3†). The surface area and pore volume of bare TPU films, MIL-88A powders and MIL-88A@TPU films are summarized in Table S2.† The BET surface area of MIL-88A powders is 281 $m^2\ g^{-1}$, which is basically consistent with the reported.[38] In addition, for the prepared mixed matrix films, the sample with the highest surface area is the 70MIL-88A@TPU film with a 32.87 $m^2\ g^{-1}$, which indicates that the porosity of the MIL-88A has been retained in these composite films. These findings clearly demonstrate that both the microstructure and the porosity of MIL-88A have been preserved in the composite films.

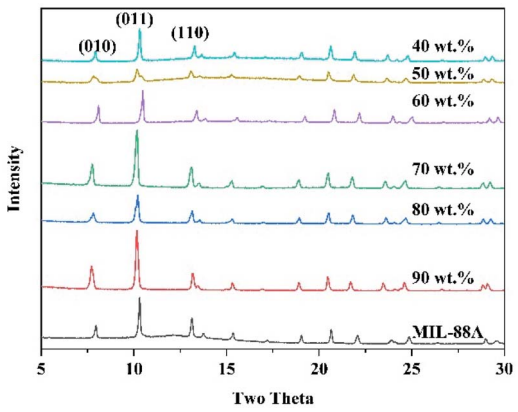

Fig. 3 XRD patterns of the pristine MIL-88A powders and MIL-88A@TPU films with different MIL-88A loadings.

Humidity responsibility of the MIL-88A@TPU films

It is well known that a saturated solution of salt at a constant temperature is equivalent to a fixed humidity value. Hence we selected the simulated salt solutions instead of ambient humidity response to examine its humidity sensitivity (seen in Table S1†).[57] According to the relative humidity table of the saturated salt solution, the saturated $MgCl_2$, K_2CO_3, NaBr, NaCl, and KCl aqueous solutions were prepared, respectively and placed in sequence in an electric blast oven at a constant temperature of 30 °C.

To find the optimal MIL-88A content, the influence of MIL-88A particles loading contents on the moisture response of the MIL-88A@TPU films was firstly studied. Two important parameters (recoverability and curl ability) for humidity actuators are considered to evaluate moisture responsibility. Fig. 4a is the humidity response results of three MIL-88A@TPU films with different MIL-88A loadings (40 wt%, 60 wt% and 80 wt%, respectively) under various humidity conditions for 10 min. The RH in the humidity actuator testing experiments was increased from 32% RH to 83% RH. It is found that the bending degree of each composite film sample increases with the increase of RH. In addition, it is noteworthy that all the composite films respond in the same curl direction, curving from the bottom surface in contact with the quartz substrate used in film preparation to the upper. To our surprise, the 60MIL-88A@TPU film showed the best humidity response ability. When the MIL-88A loading content is less than 60 wt%, the more MIL-88A content in the composite film, the greater the degree of bending under the same humidity condition. However, when the loading content of MIL-88A in the composite film is greater than 60 wt%, the bending degree of the composite film becomes smaller, and even the composite film with the content of 80 wt% does not show obvious bending phenomenon when the RH is low. All of the composite films can quickly return to their flat state after heating, which endows them with reversible and reusable ability. In order to assess the change in the bending degree of the composite film during the humidity response, the rotation angle (θ) of the composite film was measured from the video shot (seen in Fig. 4b) and the curvature k was calculated by the following formula:

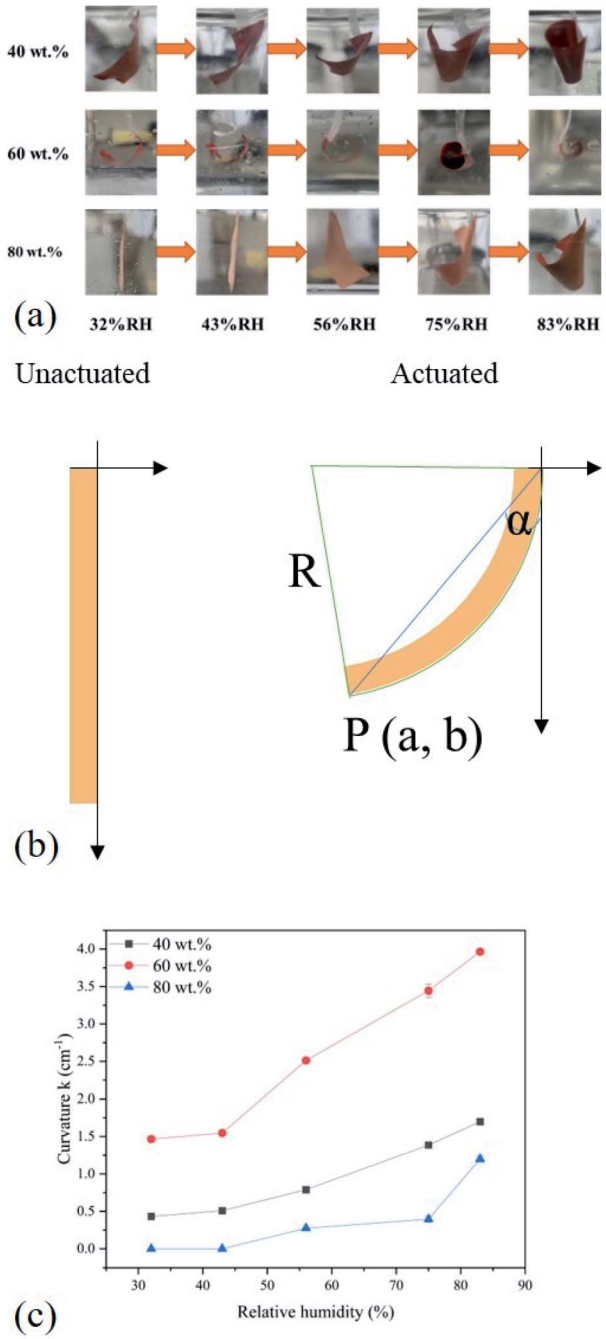

Fig. 4 (a) Digital pictures of curl process of humidity actuators with different MIL-88A loadings (40 wt%, 60 wt% and 80 wt%) at relative humidity variation. (b) Schematic diagram for the calculation of the rotation angle (θ) of the MIL-88A@TPU films (not drawn to scale). (c) Dependent of bending curvature on ΔRH for the MIL-88A@TPU films with MIL-88A loadings of 40 wt%, 60 wt% and 80 wt% (exposure time was 10 min).

$$k = \frac{\pi}{180^\circ}\frac{\theta}{L} \quad (1)$$

where θ is the bending angle and L is the free bending length of composite film. In the experiment, L is about 2.50 cm. The trend of the curvature as a function of RH presented in Fig. 4c shows that for the three composite films the curvature increases very slowly until the RH up to 43% RH, surges when the humidity is 56% RH and further increases up to a maximum, respectively. Besides, compared to the other two composite films (40MIL-88A@TPU and 80MIL-88A@TPU), the 60MIL-88A@TPU composite film exhibits a more intense bending phenomenon. Its curvature increases sharply when the RH is greater than 56% RH, and finally reaches a maximum of 3.97, which is about four times that of the 80MIL-88A@TPU film at 83% RH. When the RH is low (RH ≤43%), the curvature of the 60MIL-88A@TPU film is almost three times that of the 40MIL-88A@TPU film, while it is unexpected that the 80MIL-88A@TPU film has almost no significant bending and the curvature is basically 0.

The above experimental results show that the bending response of the humidity actuator under humidity condition is the result of the combined effect of TPU and MIL-88A crystal particles. Due to the inherent breathing effect of MIL-88A MOFs, we speculate the main reason for this curl phenomenon is that the MIL-88A crystal particles expand after absorbing water molecules from the surrounding moisture environment and thus generate stress inside the MIL-88A@TPU film. The uneven vertical gradient distribution of TPU phase in the composite film results in unbalanced stress distribution, so that the composite film curls from the bottom up (seen in Fig. 5). The FESEM images of the top and bottom of the MIL-88A@TPU films with different MIL-88A loadings (40 wt%, 60 wt%, and 80 wt%, respectively seen in Fig. 6a–f) and EDS mapping results of the cross-section of the 60MIL-88A@TPU film (seen in Fig. 6g–l) further reveal our hypothesis. When the loading of MIL-88A crystal particles is less than 60 wt%, the breath effect of MIL-88A becomes more obvious with the gradual increase of MIL-88A content in the composite film. The TPU phase wraps around the crystal particles can effectively transfer the stress caused by crystal expansion, thus causing the composite film to curl. However, when the loading content of MIL-88A exceeds 60 wt%, a large number of large pores appears in the composite film (seen in Fig. 6e and f). The expansion of the MIL-88A particles allows these large pores to be filled without excessive stress transfer. The content of TPU in the composite film is too little to transfer the stress caused by

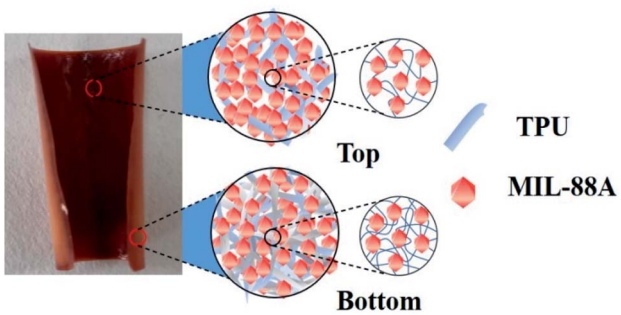

Fig. 5 Schematic illustration of the bending of a MIL-88A@TPU film after expansion at 40% RH, 60% RH and 80% RH and the vertical gradient distribution of TPU phase.

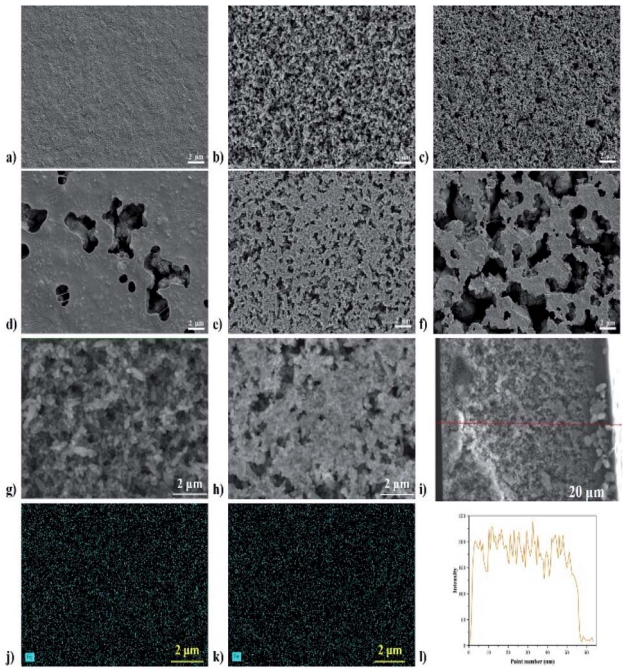

Fig. 6 FESEM images of (a–c) upper, (d–f) bottom of the MIL-88A@TPU films with different MIL-88A loadings ((a and d) are 40 wt%, (b and e) are 60 wt%, (c and f) are 80 wt%).FESEM images of (g) upper, (h) bottom of the MIL-88A@TPU films with 60 wt% MIL-88A loading and EDS mapping of Fe element distributed on the (j) upper, (k) bottom; (i) FESEM images and (l) EDS linear analyse of Fe element distributed on the cross-section of the MIL-88A@TPU films with 60 wt% MIL-88A loading.

crystal expansion of MIL-88A crystal particles after absorbing water molecules. In contrast, the TPU phase is mainly located in the region close to the bottom layer, as indicated by comparing the FESEM images of the upper and bottom of each MIL-88A@TPU film (seen in Fig. 6a–f). The main reason for this phenomenon is attributed to the low attraction interactions between TPU and MIL-88A crystals and the strong attraction interactions between TPU and quartz substrate. The TPU segment density nearby the TPU/substrate interface layer increases when dropping into quartz substrate, while the TPU segment density of the interlayer changes in the opposite way. More and more TPU segments in the interlayer region diffuse to the interlayer region of TPU/substrate, resulting in a vertical gradient distribution of TPU segment in the MIL-88A@TPU film. These results have proved that the composite films with a gradient distribution of TPU phase are beneficial for the deformation of humidity response. Therefore, use of our method will provide a new route and insight for fabricating flexible humidity actuators.

Next, on the basis of the above systematic studies, we further investigate the effects of the contact time and cycling times on the humidity response sensitivity of the MIL-88A@TPU films using 60MIL-88A@TPU. For the comprehensive consideration of economic cost and humidity sensing performance, a batch of 60MIL-88A@TPU films were exposed to the above series of saturated salt solutions. As shown in Fig. 7a, when the RH is low the curvature of the composite film does not change much, basically floating around 1.5 cm^{-1}. But as the RH is increased, the composite films exhibit a bending motion by absorbing the water molecules continuously. The final curvature increases progressively from 1.5 cm^{-1} to 4.0 cm^{-1} within 10 min as the RH is increased from 32% to 83%. For the reproducibility test, we also tested that the change in the curvature of the composite films upon dried at 80 °C and then exposured to NaCl saturated salt atmosphere to absorb water molecules for 20 cycles. The results shown in Fig. 7b, demonstrate that the self-folding capacity of the MIL-88A@TPU film are maintained. This stability in response to humidity is conducive to a wide range of industrial applications.

To demonstrate the possibility of the practical applications of the MIL-88A@TPU films, a self-folding MIL-88A@TPU strip (length: 2.5 cm; width: 0.8 cm) that can walk as the humidity is cycled was fabricated (seen in Fig. 8a, b and Video S1†). On one hand, we found that when the composite film was immersed into water, it curled instantaneously and curled within five seconds, and then unfolded slowly for three minutes (seen in

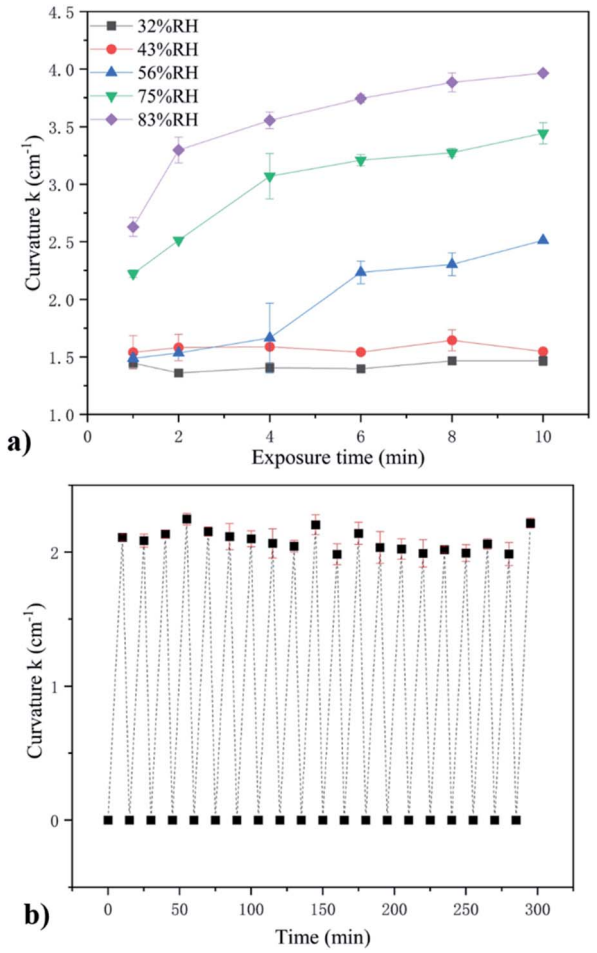

Fig. 7 (a) Dependence of changes in curvature of the MIL-88A@TPU on ΔRH with different contact time. (b) Dependent of bending curvature on ΔRH for MIL-88A@TPU films with MIL-88A loadings of 60 wt% (exposure time is 10 min and cycle 20 times).

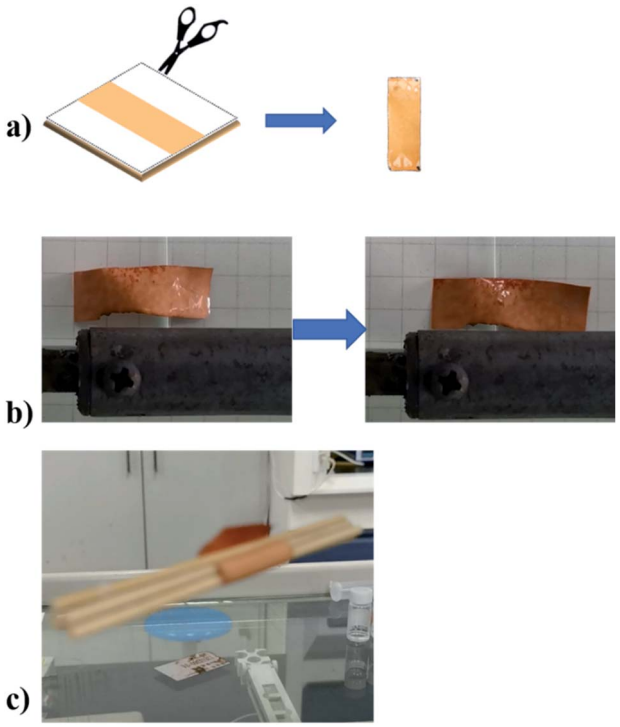

Fig. 8 (a) Schematic representation of the fabrication of the self-folding MIL-88A@TPU strip. (b) Self-walking of the MIL-88A@TPU strip driven by changing the environmental humidity. (c) Photographs of a MIL-88A@TPU film lifting cargo that is two-times heavier, upon exposure to water vapour.

Video S2†). On the other hand, in order to speed up the 2D to 3D transformations of the MIL-88A@TPU strip, we placed a heating rod next to the composite film. The results show that the MIL-88A@TPU strip exhibits unidirectional motion when exposed to the change of RH and its crawling speed is approximately 0.083 mm s^{-1}. When the RH increases, the strip bends symmetrically, while it stretches forward when the humidity decreases along the smooth glass. Meanwhile, to study its load-bearing capacity, a MIL-88A@TPU film was suspended and exposed to water vapour, the composite film was able to lift the object that is two times heavier at least (seen in Fig. 8c and Video S3†). We conclude that our composite films exhibit highly sensitive and reversible macroscopic deformations. As a result, it shows potential applications in areas such as humidity sensing or soft robotics.

Conclusions

In summary, we have successfully fabricated a humidity-driven actuator which called MIL-88A@TPU films by incorporating flexible MIL-88A crystals into TPU matrix. It can respond to the change of ambient humidity by self-folding, and shows good stability under the condition of relative humidity of 75%. In addition, the experimental results show that the exposure time and the content of MIL-88A have a great influence on the moisture response performance of the composite films. The composite films curl from the bottom up, which is attributed the uneven vertical gradient distribution of TPU phase in the composite film resulting an unbalanced stress distribution. We think this simple design has promised a new insight and route to humidity actuators and a wide range of practical applications in the fields of humidity sensing and soft robots.

Author contributions

Yi He: conceptualization, methodology, formal analysis, investigation, and writing & editing. Jiayu Guo: conceptualization, methodology, formal analysis, investigation, resources, writing & editing, and supervision. Xiazhen Yang: formal analysis, and resources. Bing Guo: formal analysis, and supervision. Hangyan Shen: resources.

Conflicts of interest

There are no conflicts to declare.

Acknowledgements

This work is partially supported by the Natural Science Foundation of Zhejiang (LQ19B060007, LY16F050005).

Notes and references

1 Y. Forterre, *J. Exp. Bot.*, 2013, **64**, 4745–4760.
2 W. Jung, W. Kim and H. Y. Kim, *Integr. Comp. Biol.*, 2014, **54**, 1034–1042.
3 M. J. Harrington, K. Razghandi, F. Ditsch, L. Guiducci, M. Rueggeberg, J. W. C. Dunlop, P. Fratzl, C. Neinhuis and I. Burgert, *Nat. Commun.*, 2011, **2**, 337.
4 C. Lv, H. Xia, Q. Shi, G. Wang, Y. S. Wang, Q. D. Chen, Y. L. Zhang, L. Q. Liu and H. B. Sun, *Adv. Mater. Interfaces*, 2017, **4**, 1601002.
5 Y. Forterre, J. M. Skotheim, J. Dumais and L. Mahadevan, *Nature*, 2005, **433**, 421–425.
6 J. R. Capadona, K. Shanmuganathan, D. J. Tyler, S. J. Rowan and C. Weder, *Science*, 2008, **319**, 1370–1374.
7 H. Cui, Q. Zhao, L. Zhang and X. Du, *Advanced Intelligent Systems*, 2020, **2**, 2000138.
8 X. Zhang, L. Chen, K. H. Lim, S. Gonuguntla, K. W. Lim, D. Pranantyo, W. P. Yong, W. J. T. Yam, Z. Low, W. J. Teo, H. P. Nien, Q. W. Loh and S. Soh, *Adv. Mater.*, 2019, **31**, 1804540.
9 C. C. Ulloa, S. Terrile and A. Barrientos, *Appl. Sci.*, 2020, **10**, 1760.
10 B. Mazzolai, G. Meloni and A. Degl'Innocenti, *Proc. SPIE*, 2017, **10162**, 1016206.
11 M. Sitti, *Nat. Rev. Mater.*, 2018, **3**, 74–75.
12 M. Sitti, H. Ceylan, W. Q. Hu, J. Giltinan, M. Turan, S. Yim and E. Diller, *Proc. IEEE*, 2015, **103**, 205–224.
13 M. Ilami, H. Bagheri, R. Ahmed, E. O. Skowronek and H. Marvi, *Adv. Mater.*, 2021, **33**, 2003139.
14 G. Maria, M. Rafael, P. Tania, D. C. Marco, F. Judith, Z. Giulia and S. Samuel, *Science Robotics*, 2021, **6**, eabe7577.

15 M. Garrad, G. Soter, A. T. Conn, H. Hauser and J. Rossiter, *Science Robotics*, 2019, **4**, eaaw6060.
16 S. Y. Zhang, A. M. Bellinger, D. L. Glettig, R. Barman, Y. A. L. Lee, J. H. Zhu, C. Cleveland, V. A. Montgomery, L. Gu, L. D. Nash, D. J. Maitland, R. Langer and G. Traverso, *Nat. Mater.*, 2015, **14**, 1065–1071.
17 T. S. Shim, S. H. Kim, C. J. Heo, H. C. Jeon and S. M. Yang, *Angew. Chem., Int. Ed.*, 2012, **51**, 1420–1423.
18 S. Y. Park, Y. H. Kim, S. Y. Lee, W. Sohn, J. E. Lee, D. H. Kim, Y. S. Shim, K. C. Kwon, K. S. Choi, H. J. Yoo, J. M. Suh, M. Ko, J. H. Lee, M. J. Lee, S. Y. Kim, M. H. Lee and H. W. Jang, *J. Mater. Chem. A*, 2018, **6**, 5016–5024.
19 Y. F. Zhang, L. Wu, X. F. Wang, J. Y. Yu and B. Ding, *Nat. Commun.*, 2020, **11**, 3302.
20 S. H. Lin, Z. Wang, X. Y. Chen, J. Ren and S. J. Ling, *Adv. Sci.*, 2020, **7**, 1902743.
21 Q. N. Zhao, Z. Yuan, Z. H. Duan, Y. D. Jiang, X. Li, Z. M. Li and H. L. Tai, *Sens. Actuators, B*, 2019, **289**, 182–185.
22 X. S. Fan, J. Y. Chung, Y. X. Lim, Z. B. Li and X. J. Loh, *ACS Appl. Mater. Interfaces*, 2016, **8**, 33351–33370.
23 A. de Leon, A. C. Barnes, P. Thomas, J. O'Donnell, C. A. Zorman and R. C. Advincula, *ACS Appl. Mater. Interfaces*, 2014, **6**, 22695–22700.
24 D. H. Gracias, *Curr. Opin. Chem. Eng.*, 2013, **2**, 112–119.
25 G. Stoychev, S. Zakharchenko, S. Turcaud, J. W. C. Dunlop and L. Ionov, *ACS Nano*, 2012, **6**, 3925–3934.
26 T. S. Wang, M. Farajollahi, Y. S. Choi, I. T. Lin, J. E. Marshall, N. M. Thompson, S. Kar-Narayan, J. D. W. Madden and S. K. Smoukov, *Interface Focus*, 2016, **6**, 20160026.
27 P. Thummala, H. Schneider, Z. Zhang, M. A. E. Andersen and R. Sarban, *IEEE/ASME Transactions on Mechatronics*, 2016, **21**, 1496–1508.
28 D. D. Sun, J. Z. Zhang, H. P. Li, Z. Y. Shi, Q. Meng, S. R. Liu, J. Z. Chen and X. Y. Liu, *Polymers*, 2021, **13**, 1889.
29 A. Dallinger, P. Kindlhofer, F. Greco and A. M. Coclite, *ACS Appl. Polym. Mater.*, 2021, **3**, 1809–1818.
30 L. Zhang, X. Qiu, Y. Yuan and T. Zhang, *ACS Appl. Mater. Interfaces*, 2017, **9**, 41599–41606.
31 G. Cai, J.-H. Ciou, Y. Liu, Y. Jiang and P. S. Lee, *Sci. Adv.*, 2019, **5**, eaaw7956.
32 P. Zhou, L. Chen, L. Yao, M. Weng and W. Zhang, *Nanoscale*, 2018, **10**, 8422–8427.
33 L. Chen, M. Weng, P. Zhou, L. Zhang, Z. Huang and W. Zhang, *Nanoscale*, 2017, **9**, 9825–9833.
34 L. Chen, M. Weng, F. Huang and W. Zhang, *Sens. Actuators, B*, 2019, **282**, 384–390.
35 Y. Ma, Y. Y. Zhang, B. S. Wu, W. P. Sun, Z. G. Li and J. Q. Sun, *Angew. Chem., Int. Ed.*, 2011, **50**, 6254–6257.
36 B. Li, T. Du, B. Yu, J. van der Gucht and F. Zhou, *Small*, 2015, **11**, 3494–3501.
37 M. Zheng, T. J. Long, X. L. Chen and J. Q. Sun, *Chin. J. Polym. Sci.*, 2019, **37**, 52–58.
38 J. Troyano, A. Carne-Sanchez and D. Maspoch, *Adv. Mater.*, 2019, **31**, 1808235.
39 Y. Y. Qiu, M. T. Wang, W. Z. Zhang, Y. X. Liu, Y. V. Li and K. Pan, *Nanoscale*, 2018, **10**, 14060–14066.
40 J. Troyano, A. Carné-Sánchez, J. Pérez-Carvajal, L. León-Reina, I. Imaz, A. Cabeza and D. Maspoch, *Angew. Chem., Int. Ed.*, 2018, **57**, 15420–15424.
41 C. P. Xu, Y. Ai, T. F. Zheng and C. H. Wang, *Sens. Actuators, A*, 2020, **315**, 112288.
42 A. H. Assen, O. Yassine, O. Shekhah, M. Eddaoudi and K. N. Salama, *ACS Sens.*, 2017, **2**, 1294–1301.
43 P. H. Tong, J. Y. Liang, X. X. Jiang and J. P. Li, *Crit. Rev. Anal. Chem.*, 2020, **50**, 376–392.
44 S. Carrasco, *Biosensors*, 2018, **8**, 92.
45 W. T. Koo, J. S. Jang and I. D. Kim, *Chem*, 2019, **5**, 1938–1963.
46 Z. Y. Zhai, X. L. Zhang, X. K. Hao, B. Niu and C. J. Li, *Adv. Mater. Technol.*, 2021, 2100127.
47 H. Y. Li, S. N. Zhao, S. Q. Zang and J. Li, *Chem. Soc. Rev.*, 2020, **49**, 6364–6401.
48 T. Chalati, P. Horcajada, R. Gref, P. Couvreur and C. Serre, *J. Mater. Chem.*, 2011, **21**, 2220–2227.
49 X. C. Cai, J. Lin and M. L. Pang, *Cryst. Growth Des.*, 2016, **16**, 3565–3568.
50 T. Calvo-Correas, L. Ugarte, P. J. Trzebiatowska, R. Sanzberro, J. Datta, M. A. Corcuera and A. Eceiza, *Polym. Degrad. Stab.*, 2017, **144**, 411–419.
51 P. Horcajada, T. Chalati, C. Serre, B. Gillet, C. Sebrie, T. Baati, J. F. Eubank, D. Heurtaux, P. Clayette, C. Kreuz, J. S. Chang, Y. K. Hwang, V. Marsaud, P. N. Bories, L. Cynober, S. Gil, G. Férey, P. Couvreur and R. Gref, *Nat. Mater.*, 2010, **9**, 172–178.
52 X. Cai, J. Lin and M. Pang, *Cryst. Growth Des.*, 2016, **16**, 3565–3568.
53 L. Yi, H. Yumin, X. Aiping, Q. Huajiao and L. Liangliang, *Nanomaterials*, 2019, **9**, 51.
54 M. S. Denny and S. M. Cohen, *Angew. Chem., Int. Ed.*, 2015, **54**, 9029–9032.
55 W.-T. Xu, L. Ma, F. Ke, F.-M. Peng, G.-S. Xu, Y.-H. Shen, J.-F. Zhu, L.-G. Qiu and Y.-P. Yuan, *Dalton Trans.*, 2014, **43**, 3792–3798.
56 C. Mellot-Draznieks, C. Serre, S. Surblé, N. Audebrand and G. Férey, *J. Appl. Chem. Sci.*, 2005, **127**, 16273–16278.
57 A. Carotenuto and M. Dell'Isola, *Int. J. Thermophys.*, 1996, **17**, 1423–1439.